Physical properties and crystal structure analysis of double-perovskite $NdBaMn_2O_6$ by using single crystals

S. Yamada,[1] H. Sagayama,[2,3] K. Higuchi,[1] T. Sasaki,[1] K. Sugimoto,[4] and T. Arima[5]

[1]*Department of Materials System Science, Yokohama City University, Yokohama 236-0027, Japan*

[2]*Institute of Materials Structure Science, High Energy Accelerator Research Organization, Tsukuba, Ibaraki 305-0801, Japan*

[3]*Department of Materials Structure Science, The Graduate University for Advanced Studies, Tsukuba, Ibaraki 305-0801, Japan*

[4]*SPring-8/JASRI, Kouto, Sayo, Hyogo 679-5198, Japan*

[5]*Department of Advanced Materials Science, The University of Tokyo, Kashiwa 277-8561, Japan*

(Received 3 March 2016; revised manuscript received 29 November 2016; published 3 January 2017)

We have succeeded in growing large single crystals of double-perovskite $NdBaMn_2O_6$ with the c axis aligned, and carried out a crystal structure analysis and measurements of resistivity and magnetization. A first-order metal-insulator transition at $T_{MI} \simeq 290$ K is accompanied by a large jump of magnetization and lattice constants. The distortion of MnO_6 octahedra is consistent with a ferroic orbital order of x^2-y^2 type, although other orbital orders cannot be completely discarded. Néel temperature T_N is determined to be 235 K, which is fairly lower than T_{MI}, on the basis of the onset of a large magnetic anisotropy. Another structural phase transition from tetragonal to orthorhombic is found at 370 K, which arises from staggered tilting of MnO_6 octahedra and little affects the transport and magnetic properties.

DOI: 10.1103/PhysRevB.95.035101

I. INTRODUCTION

Perovskitelike manganese oxide compounds have long been attracting the attention of material scientists because of the strong coupling among charge, orbital, and spin degrees of freedom [1–5]. The manganite compounds with the Mn formal valence of +3.5 often exhibit a metal-insulator transition accompanied by ordering in the charge, orbital, and spin sectors, depending on the bandwidth [6]. For example, $Pr_{0.5}Ca_{0.5}MnO_3$ undergoes a charge/orbital ordering accompanied by a metal-insulator transition at ∼230 K [7]. $Pr_{0.5}Sr_{0.5}MnO_3$, the bandwidth of which is fairly larger than $Pr_{0.5}Ca_{0.5}MnO_3$, undergoes successive phase transitions. With cooling, a transition to a ferromagnetic metal phase first takes place at ∼265 K, and then at 140 K the resistivity shows an abrupt increase caused by the x^2-y^2–type orbital ferroic ordering and a simultaneous ferromagnetic-to-layered (A-type) antiferromagnetic (AFM) transition [8]. $La_{0.5}Sr_{0.5}MnO_3$ with a further widened bandwidth exhibits only a ferromagnetic transition, and the charge and orbital sectors remain disordered [9]. A similar evolution of the electronic state with controlling the bandwidth has been also reported in $RE BaMn_2O_6$ double-perovskite systems, where RE is a trivalent rare earth [10–22]. In the double-perovskite manganites, RE and barium atoms are regularly arranged to remove the randomness [see insets of Fig. 1(d)]. Physical properties of the double-perovskite manganites depend on the ionic radius of RE. For instance, when the ionic radius is smaller than or equal to that of Sm, charge- and orbital-ordering states are stabilized below a temperature higher than room temperature [18,20]. On the other hand, for RE = La or Pr, the charge ordering does not take place at any temperature. The A-type AFM and ferromagnetic (FM) phases instead appear at low temperatures [16]. It has been reported that $NdBaMn_2O_6$ is located close to the boundary between the charge-/orbital-ordered phase, the charge-disordered orbital-ordered A-type AFM phase, and FM phase. Such a phase competition may provide us a ground for developing a new functionality. However, experimental studies were performed on polycrystalline samples so far, which prevents a deep understanding of its physical properties. For example, the onset of the A-type antiferromagnetic order was determined by the magnetic susceptibility and neutron diffraction of a polycrystalline sample. However, it is well known that the change of orbital state would also affect the magnetic property [23]. The neutron diffraction could not give clear evidence, because the A-type antiferromagnetic order does not give rise to superlattice in the double perovskite, and orbital order itself could modify the intensities of diffraction peaks. The anisotropy in the magnetic property may provide useful information on the magnetic order. In this paper, we study the magnetic, electric, and structural properties using crystals of $NdBaMn_2O_6$ with the c axis perfectly aligned.

II. EXPERIMENTAL

Single crystals of $NdBaMn_2O_6$ were grown by the floating zone (FZ) method. Powders of Nd_2O_3, $BaCO_3$, and Mn_3O_4 were mixed, ground, and calcined at 1290 °C for 48 h in Ar (6 N) atmosphere, and then pulverized. The resultant powder was shaped into a cylinder under a hydrostatic pressure of 30 MPa and sintered at 1290 °C for 12 h in Ar (6 N) atmosphere to form feeding and seeding rods. An FZ furnace equipped with two halogen incandescent lamps and hemielliptic focusing mirrors was used for the crystal growth. The molten zone was vertically scanned at a rate of 2 mm/h in Ar gas mixed with a tiny portion ($\leqslant$0.1%) of H_2. The melt-grown bar was annealed in O_2 atmosphere at 500 °C for 48 h. In order to measure anisotropic properties, we cut the crystal boules into some pieces, and the orientation of the c axis was determined by x-ray diffraction. Laue photographs confirmed that every sample was a single crystal. Magnetization was measured using a commercial superconducting quantum interface device magnetometer (Quantum Design MPML-XL). The electrical resistivity was measured by a conventional four-probe method.

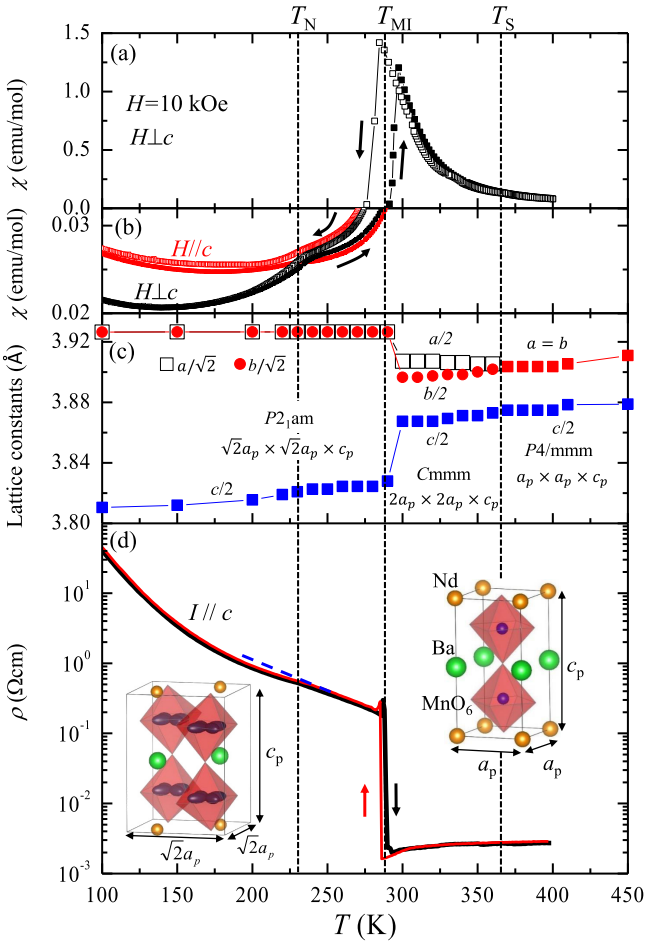

FIG. 1. Temperature dependence of (a) magnetic susceptibility in $H \perp c$, (b) magnetic anisotropy, (c) lattice constants, and (d) electrical resistivity in $NdBaMn_2O_6$. The magnetic susceptibilities were measured in a magnetic field of 10 kOe. T_S and T_{MI} are structural phase transition temperatures. T_N denotes Néel temperature. A broken line in (d) is a visual guide.

Single-crystal synchrotron x-ray diffraction was performed at SPring-8, Japan. A single crystal was crashed into small grains, and a grain of dimension 50 μm × 10 μm × 10 μm was selected for the measurement. The incident x-ray beam was monochromatized by using Si(311) double crystals. The wavelength was calibrated to be 0.357 25 Å using a powder diffraction pattern of CeO_2. X-ray diffraction intensity data were collected with a cylindrical imaging-plate diffractometer. The temperature was controlled by using a He-gas spray-type controller. The RAPID-AUTO program developed by Rigaku Corp. was used to index reflections, calculate their integrated intensities, and correct the absorption effect by applying a semiempirical method. The WINGX with a built-in SHELXL program was used for refining the structural parameters [24,25]. Charge disproportionation and anisotropic orbital shapes of Mn ions were evaluated from local breathing (Q_1) and Jahn-Teller distortion (Q_2, Q_3) modes of an MnO_6 octahedron, respectively. The valence state V of each Mn ion was evaluated by the valence-bond-sum method, expressed as $V = \sum_i \exp[(d_0 - d_i)/B]$, where d_i is the distance between the Mn ion and the ith coordinate oxygen ion. B and d_0 are empirical parameters of $B = 0.37$ Å and $d_0 = 1.753$ Å [26]. To determine the $3d$-orbital shape, Kanamori representation with the normal mode analysis was applied [27].

III. RESULTS AND DISCUSSION

Figure 1 shows the temperature dependence of magnetic susceptibility, lattice constants, and electrical resistivity. Three-step successive phase transitions are clearly observed at 370 K (T_S), 290 K (T_{MI}), and 235 K (T_N). Above T_{MI}, Curie-Weiss paramagnetism and a metallic conduction are observed. We subtracted the Curie paramagnetic component of Nd^{3+} ions from the susceptibility data up to 600 K (not shown) and performed a Curie-Weiss analysis. The obtained Weiss temperature and effective magnetic moments above T_S are 350 K and 4.3 μ_B per Mn, respectively. The latter roughly agrees with the average of the effective moments of Mn^{4+} ($S = 3/2$) and Mn^{3+} ($S = 2$). In this temperature range, fundamental Bragg reflections do not show any splitting, indicating that the tetragonal symmetry is retained. We conclude that the unit cell is $a_p \times a_p \times c_p$, because no superlattice peak is observed [Fig. 3(a)]. Here a_p and c_p denote the lattice parameters of the distortion-free double-perovskite structure (see inset). Below T_S, superlattice reflections of $(h + 1/2\ \ k + 1/2\ \ l)$ appear [Fig. 3(b)] and $(h\ 0\ 0)$ peaks are split [Fig. 3(f)]. Because the ionic size of trivalent rare-earth ions is a little too small to maintain the undistorted perovskite structure in general, MnO_6 octahedra are rotated and tilted to relax the size mismatch between rare-earth and transition-metal ions. As discussed in detail later, the structural transition at 370 K originates from this sort of instability because the Q_2 and Q_3 distortions of octahedra do not change very much, but the octahedra exhibit alternate tilting around the a-axis by up to 5 degrees below T_S. The peak split becomes larger with cooling, as shown in Fig. 3(c), implying a gradual increase in the tilting of MnO_6 octahedra. In fact, apparent Weiss temperature and the effective magnetic moment between T_{MI} and T_S are changed to 310 K and 5.8 μ_B per Mn site, respectively. The changes of the

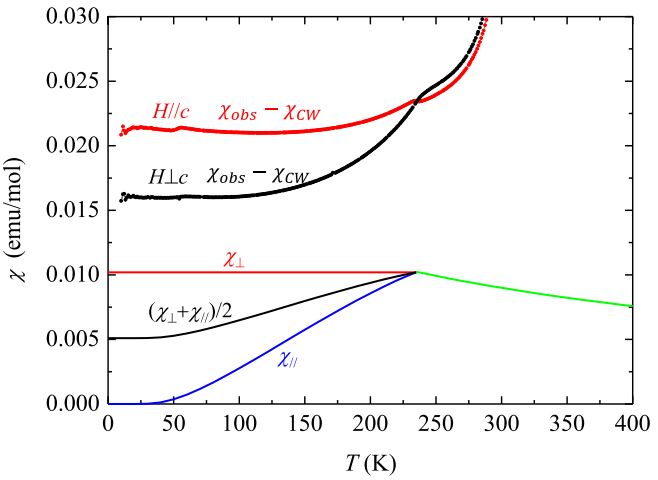

FIG. 2. Temperature dependence of anisotropic magnetic susceptibilities (χ_{obs}) after subtracting the Curie-Weiss term (χ_{CW}) in $NdBaMn_2O_6$ compared with theoretical curves using a simple molecular-field approximation (see text).

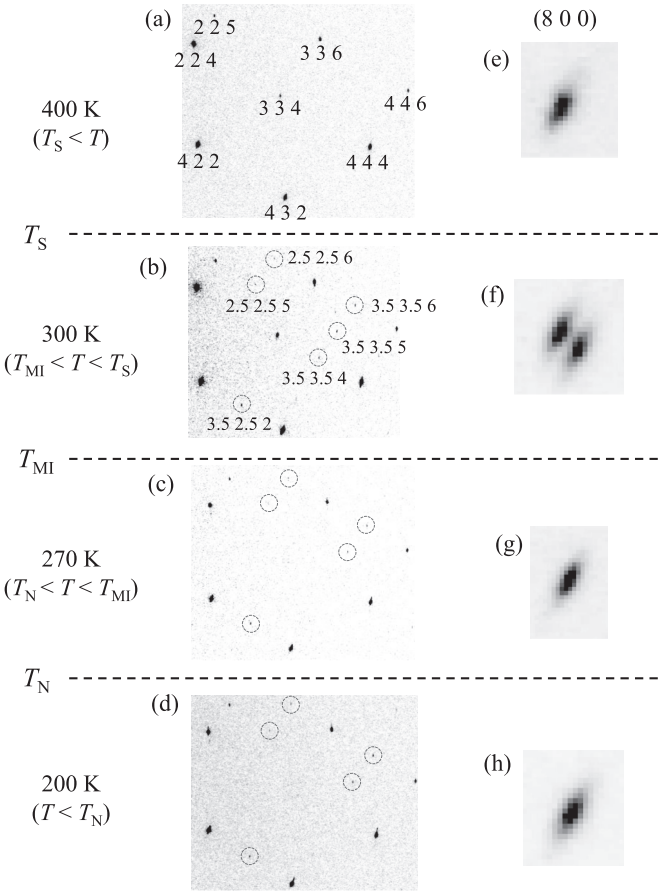

FIG. 3. X-ray oscillation photographs of $NdBaMn_2O_6$ and 8 0 0 peak profiles at (a, e) 400 K ($T_S < T$), (b, f) 300 K ($T_{MI} < T < T_S$), (c, g) 270 K ($T_N < T < T_{MI}$), and (d, h) 200 K ($T < T_N$). Dotted circles on the left panels indicate superlattice reflections.

parameters across T_S may be caused by a gradual suppression of the ferromagnetic interaction between neighboring Mn moments. At T_{MI}, a first-order transition with clear anomalies in magnetic susceptibility, lattice constants, and resistivity is observed. The temperature dependence of lattice constants in Fig. 1(c) also suggests that MnO_6 octahedra below T_{MI} should be distorted in the oblate shape, which is strongly coupled with the x^2-y^2 orbital. This phase transition is clearly characterized by the sudden enhancement (not the onset) of the orbital order as well as a metal-insulator transition.

In previous studies using polycrystalline samples, T_{MI} was assigned to the orbital and spin-ordering temperature [16,18]. However, the onset temperature of magnetic anisotropy is not 290 K but 235 K [Fig. 1(b)]. We further analyzed the anisotropic magnetic susceptibility as follows. First we fitted the low-temperature data below 100 K to Curie-Weiss susceptibility. The effective magnetic moment as estimated from the Curie-Weiss term below 100 K is 2.2 μ_B, which is smaller than that of an isolated Nd^{3+} ion (=3.6μ_B). Figure 2 shows the temperature dependence of the magnetic susceptibilities after subtracting the Curie-Weiss part. The difference of magnetic susceptibility between in $H//c$ and in $H \perp c$ is saturated to be about 0.005 emu/mol below 100 K, and a calculation of the temperature dependence of the magnetic susceptibility based on the molecular-field approximation. In this estimation, the average spin angular moment of Mn ion is 7/4 ($Mn^{3.5+}$) and Néel temperature is 235 K. The observed magnetic susceptibility in $H \perp c$ should correspond to $(\chi_{//} + \chi_{\perp})/2$ due to the ab twin structure. The absolute value of the anisotropy agrees with the calculation quantitatively. We thus conclude that the antiferromagnetic order appears below the onset of the anisotropy, i.e., 235 K. The paramagnetic phase with ferroic orbital order between T_N and T_{MI} has not been found in other manganite compounds so far. Nakajima *et al.* reported the temperature dependence of neutron powder diffraction [16]. They observed that the intensity of the (001) diffraction was enhanced below 240 K. In our opinion, their neutron data rather support our conclusion that the magnetic transition temperature T_N should be 235 K, although they said that T_N should be 290 K, where the magnetic susceptibility steeply changed.

TABLE I. Structure parameters for $NdBaMn_2O_6$ at 450 K with $P4/mmm$ (No. 123) of tetragonal crystal symmetry. The obtained R factors are $R = 3.64\%$ and $R_w = 5.91\%$. The lattice parameters are $a = 3.911\,0(4)$ Å, $c = 7.757\,7(6)$ Å. The goodness-of-fit indicator S (all reflection) is 1.085. The obtained R factors are $R = 3.64\%$ and $R_w = 5.91\%$. The valence of Mn ions is estimated by the bond valence sum to be $V_{VBS} = 3.495$.

	Occupancy	Site	x	y	z	B_{iso}(Å^2)
Nd/Ba	0.98795/0.01205	1a	0	0	0	0.00919(5)
Ba/Nd	0.98795/0.01205	1b	0	0	0.5	0.00690(5)
Mn	1	2h	0.5	0.5	0.24579(6)	0.00490(5)
O1	1	1c	0.5	0.5	0	0.0236(1)
O2	1	1d	0.5	0.5	0.5	0.0098(5)
O3	1	4i	0	0.5	0.2274(2)	0.0134(3)
	U_{11}(Å^2)	U_{22}(Å^2)	U_{33}(Å^2)	U_{12}(Å^2)	U_{13}(Å^2)	U_{23}(Å^2)
Nd/Ba	0.01008(8)	0.01008(8)	0.00742(7)	0	0	0
Ba/Nd	0.00660(7)	0.00660(7)	0.00749(8)	0	0	0
Mn	0.00483(7)	0.00483(7)	0.00504(1)	0	0	0
O1	0.0326(2)	0.0326(18)	0.0056(9)	0	0	0
O2	0.0097(7)	0.0097(7)	0.0102(9)	0	0	0
O3	0.0085(5)	0.0146(7)	0.0170(7)	0	0	0

TABLE II. Structure parameters for $NdBaMn_2O_6$ at 300 K with $Cmmm$ (No. 65) of orthorhombic crystal symmetry. The lattice parameters are $a = 7.814\,8(1)$ Å, $b = 7.787\,7(6)$ Å, $c = 7.728\,1(12)$ Å. The goodness-of-fit indicator S (all reflection) is 0.964. The obtained R factors are $R = 3.06\%$ and $R_w = 5.98\%$. The valence of Mn ions is estimated by the bond valence sum to be $V_{VBS} = 3.526$.

	Occupancy	Site	x	y	z	B_{iso}(Å^2)
Nd/Ba	0.98795/0.01205	4g	0.25468(2)	0	0	0.00662(3)
Ba/Nd	0.98795/0.01205	4h	0.25148(2)	0	0.5	0.00533(2)
Mn	1	8n	0	0.24981(2)	0.24609(2)	0.00387(3)
O1	1	4i	0	0.2712(4)	0	0.0154(3)
O2	1	4j	0	0.2416(2)	0.5	0.0087(2)
O3	1	4k	0	0	0.2141(5)	0.0101(4)
O4	1	4l	0	0.5	0.2430(4)	0.0100(5)
O5	1	8m	0.25	0.25	0.2263(6)	0.0097(3)
	U_{11}(Å^2)	U_{22}(Å^2)	U_{33}(Å^2)	U_{12}(Å^2)	U_{13}(Å^2)	U_{23}(Å^2)
Nd/Ba	0.00759(8)	0.00687(8)	0.00540(3)	0	0	0
Ba/Nd	0.00504(9)	0.00568(10)	0.00527(4)	0	0	0
Mn	0.0047(4)	0.0034(4)	0.00358(5)	0.00002(4)	0	0
O1	0.0209(1)	0.0201(2)	0.0051(4)	0	0	0
O2	0.0076(1)	0.0103(1)	0.0081(4)	0	0	0
O3	0.0121(8)	0.0078(1)	0.0104(9)	0	0	0
O4	0.0118(7)	0.0075(1)	0.0107(9)	0	0	0
O5	0.0074(8)	0.0095(7)	0.0123(6)	0	0	0.0003(4)

As shown in Fig. 2, the observed magnetic susceptibilities are about 0.011 emu/mol larger than the calculated ones. Such a temperature-independent term may originate from the van Vleck term. The magnetic moments of Nd^{3+} ions may contribute not only to Curie paramagnetism but also to van Vleck paramagnetism in the low-temperature range due to a ligand-field splitting of the lowest $^4I_{9/2}$ multiplet.

As shown in Figs. 3(c) and 3(d), the x-ray diffraction pattern below T_N is essentially same as that in $T_N < T < T_{MI}$. The space group of crystal structure does not change across T_N. Therefore we hereafter focus the structural changes at T_S and T_{MI}. Single-crystal structure analyses were carried out at 450 K, 300 K, and 100 K. The parameter of the Nd/Ba ordering ratio was estimated to be 98.795% from the 450-K data set. This value was used as a constant for analyzing lower-temperature x-ray data, because the number of free parameters is the smallest in the high-temperature phase (HT) above T_S. As shown in Fig. 3, superlattice reflections of $(h + 1/2\ \ k + 1/2\ \ l)$ are clearly observed in the three phases below T_S [28]. The splitting of (8 0 0) reflection is discernible only in the medium-temperature (MT) phase between T_{MI} and T_S. We examined all possible space groups with the inclusion of the ab twin structures for each phase and concluded that the space groups are $P4/mmm$ (450 K), $Cmmm$ (300 K), and $P2_1am$ (100 K), respectively. The obtained structural parameters are listed in Tables I (450 K), II

TABLE III. Structure parameters for $NdBaMn_2O_6$ at 100 K with $P2_1am$ (No. 26) of orthorhombic crystal symmetry. The lattice parameters are $a = 5.555\,0(3)$ Å, $b = 5.555\,0(2)$ Å, $c = 7.621\,0(5)$ Å. The goodness-of-fit indicator S (all reflection) is 1.028. The obtained R factors are $R = 3.45\%$ and $R_w = 6.54\%$. The valence of Mn ions is estimated by bond valence sum to be $V_{VBS} = 3.510$.

	Occupancy	Site	x	y	z	B_{iso}(Å^2)
Nd/Ba	0.98795/0.01205	2a	0.7499(2)	0.24253(3)	0	0.00371(5)
Ba/Nd	0.98795/0.01205	2b	0.7491(3)	0.24832(2)	0.5	0.00344(5)
Mn	1	4c	0.2532(1)	0.24985(3)	0.24639(3)	0.00297(1)
O1	1	2a	0.2232(2)	0.2127(6)	0	0.0086(9)
O2	1	2b	0.251(3)	0.2655(5)	0.5	0.0067(4)
O3	1	4c	0.002(3)	–0.001(2)	0.2409(2)	0.0094(4)
O4	1	4c	–0.004(3)	0.5003(2)	0.2150(2)	0.0098(4)
	U_{11}(Å^2)	U_{22}(Å^2)	U_{33}(Å^2)	U_{12}(Å^2)	U_{13}(Å^2)	U_{23}(Å^2)
Nd/Ba	0.00560(2)	0.00314(6)	0.00239(5)	0	0	–0.00148(1)
Ba/Nd	0.00561(2)	0.00222(8)	0.00248(5)	0	0	–0.00043(9)
Mn	0.0040(5)	0.0028(2)	0.00214(9)	0.00006(4)	–0.0001(4)	0.0002(2)
O1	0.014(3)	0.0082(6)	0.0032(6)	0	0	0.0022(9)
O2	0.0109(1)	0.0058(5)	0.0035(5)	0	0	0.0061(2)
O3	0.0108(1)	0.0081(5)	0.0093(5)	0.002(2)	0.002(3)	0.0009(5)
O4	0.0144(1)	0.0091(5)	0.0059(4)	0.0010(2)	–0.003(2)	–0.0047(7)

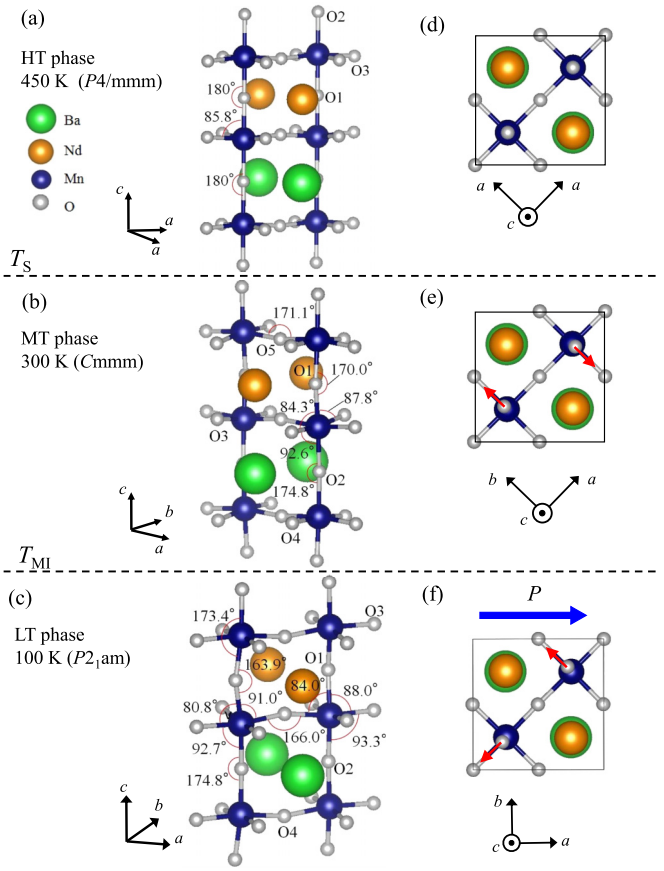

FIG. 4. Crystal structures of (a) HT, (b) MT, and (c) LT phases of $NdBaMn_2O_6$. Bond angles relevant to distortion of the MnO_6 octahedron are also shown. (d, e, f) Projections of the crystal structures onto the *ab* plane in HT, MT, and LT phases. Arrows in the projections (e) and (f) denote the oxygen displacements from the ideal double-perovskite structure. A large arrow on the projection (f) shows the polarization direction.

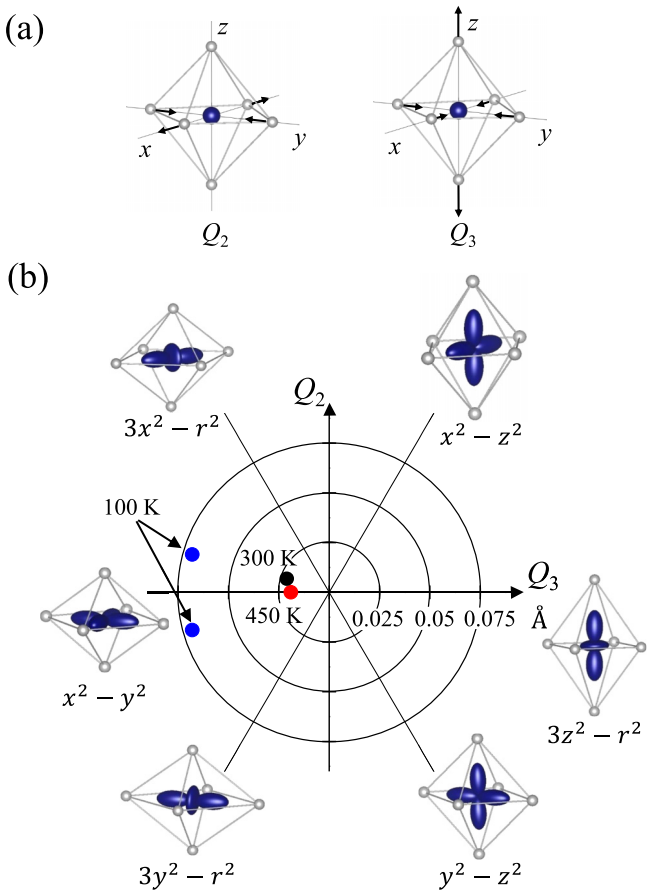

FIG. 5. (a) Schematic drawings of Q_2 and Q_3 distortion modes which directly couple with the orbital occupation in doubly degenerate e_g states. (b) Q_2-Q_3 mode analysis of the MnO_6 octahedron in $NdBaMn_2O_6$ at 100 K, 300 K, and 450 K. A stabilized orbital is also attached in each distorted octahedron.

(300 K), and III (100 K). If we assume a centrosymmetric space group *Pmam* for the low-temperature (LT) orbital-ordered antiferromagnetic (AFM) phases, the *R* factor becomes 4.87%. The difference between $P2_1am$ and *Pmam* appears in the *x* coordinate of the O1 site. The lower-symmetry-based analysis gives that $x(O1) = 0.223\ 2(2)$, which clearly deviates from the fixed value 1/4 for *Pmam*. We conclude that the space group of LT phases should be $P2_1am$, since the antiferromagnetic transition gives little impact on the x-ray data.

Figure 4 shows several bond angles which are mainly related to distortion of MnO_6 octahedra in (a) HT, (b) MT, and (c) LT phases. The amplitudes of Jahn-Teller distortion modes Q_2 and Q_3, which are schematically drawn in Fig. 5(a), of the MnO_6 octahedron in each phase are plotted in Fig. 5(b). The distortion of each MnO_6 octahedron consists of six symmetric and nine antisymmetric modes [29]. The antisymmetric modes do not give a first-order perturbation term between the 3*d* energy levels. In the HT phase above T_S, O ions in NdO and BaO layers (O1 and O2) are located at the center of two Mn ions, while O ions in MnO_2 layers are shifted along the stacking axis toward the NdO layer. This distortion of MnO_6 octahedron is likely caused by differences in radius and electric charge between Nd^{3+} and Ba^{2+} ions, as Nakajima *et al.* proposed [16].

In contrast to the large polar distortion of MnO_6 octahedra, the magnitude of the Jahn-Teller distortion in HT phase is smaller than 0.025 Å. In the MT phase, MnO_6 octahedra are alternately tilted by up to 5 degrees around the *a* axis, resulting in the shift of O1 and O2 along the *b* axis. The tilting is essentially free from Jahn-Teller distortion, indicating that the orbital sector remains disordered. The Jahn-Teller distortion starts to increase below T_{MI} and reaches about 0.07 Å at 100 K. We hence conclude that the orbital occupation should change at T_{MI}. It is of note that the Jahn-Teller distortion in the insulator phase is smaller than those for Mn^{3+} in the charge-ordering phase of other perovskite-type manganites, e.g., $SmBaMn_2O_6$ ($\simeq$0.2) [30], $Pr_{0.5}Ca_{0.5}MnO_3$ ($\simeq$0.1) [31], $Eu_{0.5}Ca_{1.5}MnO_4$ ($\simeq$0.08) [31]. This should be attributed to the absence of charge ordering in $NdBaMn_2O_6$. The analysis of the amplitude of the Q_2 and Q_3 modes suggests that the orbital shape in the LT phase is approximately x^2-y^2, as schematically shown in Fig. 1(d). This orbital ordering is consistent with A-type AFM ordering determined by powder neutron diffraction [16]. Here, one should note that the distortion mode analysis does not provide direct evidence of the orbital occupation. Some further studies are necessary to determine the accurate orbital shape, while there is no established method to give

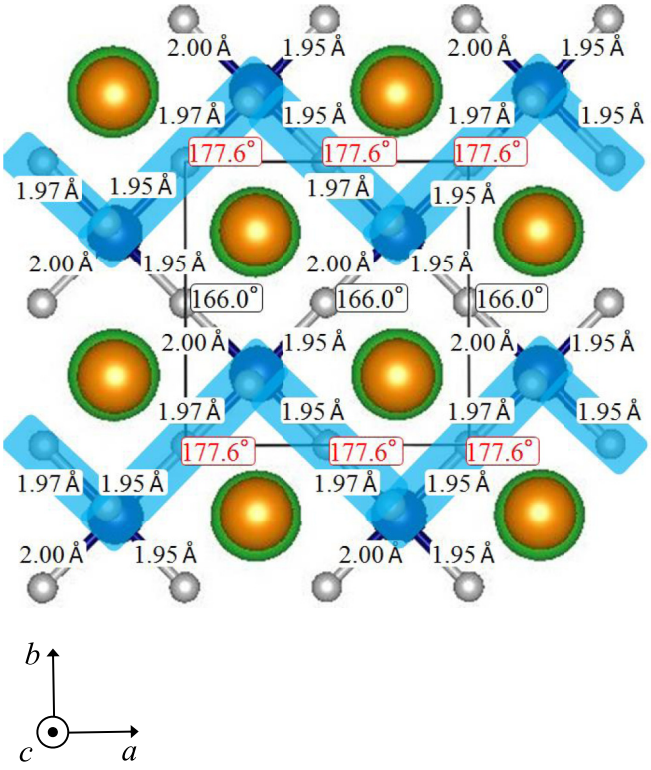

FIG. 6. Mn-O-Mn bond angles and lengths in the MnO_2 layer in LT phase.

conclusive information [32–34]. A first-principles calculation of the electronic state would also provide useful information.

In general, the electrical resistivity of the A-type AFM phase with the x^2-y^2 orbital order is metallic within the ab plane [35]. In contrast, our preliminary data suggest that the temperature dependence of electrical resistivity in the ab plane is insulating below T_{MI}. As shown in Fig. 6, there are two kinds of the Mn-O-Mn bonds on (001) MnO_2 layers in the LT phase. Half are almost straight (177.6 degrees) while the other half are heavily bent (166.0 degrees). The former bonds compose larger-transfer Mn zigzag chains. The electron conduction in the MnO_2 plane with such a large anisotropy can be much reduced than in the case of a regular square lattice. In addition, our samples are subject to the ab twin structure in the LT phase. The combination of the one-dimensional conduction path and the ab twin structure could induce a semiconducting behavior. In metallic orbital-ordering phase with the A-type antiferromagnetism in $Nd_{0.45}Sr_{0.55}MnO_3$, Mn-O-Mn bonds of the MnO_2 layer are identical [8], which hosts the two-dimensional metallic conduction.

Finally, we discuss the evolution of the tilt of MnO_6 octahedra. MnO_6 octahedra are not tilted at all in the HT phase. The tilting about 5 degrees around the a axis is observed in the MT phase. The tilting angle increases up to 10 degrees in the LT phase. Here it should be noted that the tilting direction in the LT phase is different by 45 degrees from that in MT phase. The MnO_6 tiltings are mainly driven by the displacements of the oxygen ions (O1) in NdO layers, as schematically depicted in Fig. 4. The oxygen ions (O1, O2) in NdO and BaO layers in HT phase are not shifted from the center of two neighboring Mn ions at all, whereas O1 and O2 in the MT phase are alternately displaced by 0.17 Å and 0.07 Å along the b axis. The displacements of O1 in the NdO layer of 0.25 Å are not canceled out in the LT phase, which hosts the noncentrosymmetric nature. The oxygen ions (O2) in the BaO layer are less displaced (−0.09 Å). The spontaneous electric polarization along the a axis is estimated to be 6.0 $\mu C/cm^2$ in the simple point-charge approximation. This value is even larger than that of the low-temperature charge-ordered phase in $SmBaMn_2O_6$ (1.32 $\mu C/cm^2$) [30]. As schematically drawn in Figs. 4(e) and 4(f), the polarization in $NdBaMn_2O_6$ is mainly ascribed to the displacement of oxygen ions in NdO layers, whereas in $SmBaMn_2O_6$ the displacement of oxygen ions in charge-ordered MnO_2 layers dominantly contributes to the polarization. The presence of spontaneous polarization has not been experimentally confirmed, mainly due to the low electrical resistivity of this material. Optical second-harmonic generation could detect the spontaneous symmetry breaking in the near future [36].

IV. CONCLUSION

The temperature evolution of the electronic and crystallographic properties in $NdBaMn_2O_6$ single crystal has been revealed. The metal-insulator transition at $T_{MI} \simeq 290$ K is caused by a crystal structure phase transition coupled with an orbital order transition. All the Mn sites are crystallographically equivalent in every phase, indicating the absence of charge ordering. The magnetic susceptibility suddenly decreases in the orbital-ordered phase. Spatial inversion symmetry is broken by the orbital order. The Néel temperature is determined to be $T_N = 235$ K from the onset of the magnetic anisotropy.

ACKNOWLEDGMENTS

This study was partly supported by a Grant-in-Aid for Scientific Research (Grant No. 24540380) from the Japan Society for the Promotion of Science and by the Strategic Research Promotion Program (Grant No. G2503) of Yokohama City University. Crystal structures are drawn by using the program VESTA [37]. Synchrotron x-ray diffraction measurements were performed at SPring-8, Japan (Proposals No. 2013A1005, No. 2013B1006, and No. 2014A1339).

[1] K. Chahara, T. Ohno, M. Kasai, and Y. Kozono, Appl. Phys. Lett. **63**, 1990 (1993).
[2] R. von Helmolt, J. Wecker, B. Holzapfel, L. Schultz, and K. Samwer, Phys. Rev. Lett. **71**, 2331 (1993).
[3] Y. Tokura, A. Urushibara, Y. Moritomo, T. Arima, A. Asamitsu, G. Kido, and N. Furukawa, J. Phys. Soc. Jpn. **63**, 3931 (1994).
[4] H. Kuwahara, Y. Moritomo, Y. Tomioka, A. Asamitsu, M. Kasai, R. Kumai, and Y. Tokura, Phys. Rev. B **56**, 9386 (1997).

[5] Y. Tokura and Y. Tomioka, J. Magn. Magn. Mater. **200**, 1 (1999).
[6] P. M. Woodward, T. Vogt, D. E. Cox, A. Arulraj, C. N. R. Rao, P. Karen, and A. K. Cheetham, Chem. Mater. **10**, 3652 (1998).
[7] Y. Tomioka, A. Asamitsu, H. Kuwahara, Y. Moritomo, and Y. Tokura, Phys. Rev. B **53**, R1689 (1996).
[8] H. Kawano, R. Kajimoto, H. Yoshizawa, Y. Tomioka, H. Kuwahara, and Y. Tokura, Phys. Rev. Lett. **78**, 4253 (1997).
[9] A. Urushibara, Y. Moritomo, T. Arima, A. Asamitsu, G. Kido, and Y. Tokura, Phys. Rev. B **51**, 14103 (1995).
[10] F. Millange, V. Caignaert, B. Domengès, B. Raveau, and E. Suard, Chem. Mater. **10**, 1974 (1998).
[11] V. Caignaert, F. Millange, B. Domengès, B. Raveau, and E. Suard, Chem. Mater. **11**, 930 (1999).
[12] S. V. Trukhanov, I. O. Troyanchuk, M. Hervieu, H. Szymczak, and K. Bärner, Phys. Rev. B **66**, 184424 (2002).
[13] T. Nakajima, H. Kageyama, and Y. Ueda, J. Phys. Chem. Solids **63**, 913 (2002).
[14] A. J. Williams and J. P. Attfield, Phys. Rev. B **66**, 220405(R) (2002).
[15] T. Arima, D. Akahoshi, K. Oikawa, T. Kamiyama, M. Uchida, Y. Matsui, and Y. Tokura, Phys. Rev. B **66**, 140408(R) (2002).
[16] T. Nakajima, H. Kageyama, H. Yoshizawa, K. Ohoyama, and Y. Ueda, J. Phys. Soc. Jpn. **72**, 3237 (2003).
[17] H. Kageyama, T. Nakajima, M. Ichihara, Y. Ueda, H. Yoshizawa, and K. Ohoyama, J. Phys. Soc. Jpn. **72**, 241 (2003).
[18] D. Akahoshi, M. Uchida, Y. Tomioka, T. Arima, Y. Matsui, and Y. Tokura, Phys. Rev. Lett. **90**, 177203 (2003).
[19] T. Nakajima, H. Yoshizawa, and Y. Ueda, J. Phys. Soc. Jpn. **73**, 2283 (2004).
[20] D. Akahoshi, Y. Okimoto, M. Kubota, R. Kumai, T. Arima, Y. Tomioka, and Y. Tokura, Phys. Rev. B **70**, 064418 (2004).
[21] T. Nakajima and Y. Ueda, J. Appl. Phys. **98**, 046108 (2005).
[22] T. Nakajima, Ph.D. thesis, the University of Tokyo, 2006.
[23] S. Yamada, T. Matsunaga, E. Sugano, H. Sagayama, S. Konno, S. Nishiyama, Y. Watanabe, and T.-h. Arima, Phys. Rev. B **75**, 214431 (2007).
[24] L. J. Farrugia, J. Appl. Crystallogr. **45**, 849 (2012).
[25] G. M. Sheldrick, Acta Crystallogr., Sect. A: Found. Crystallogr. **64**, 112 (2008).
[26] I. D. Brown and D. Altermatt, Acta Crystallogr., Sect. B: Struct. Sci. **41**, 244 (1985).
[27] J. Kanamori, J. Appl. Phys. **31**, S14 (1960).
[28] See Fig. S1 in the Supplemental Material at http://link.aps.org/supplemental/10.1103/PhysRevB.95.035101 for the temperature dependence of diffraction intensities of superlattice and fundamental peaks.
[29] See Table SI in the Supplemental Material at http://link.aps.org/supplemental/10.1103/PhysRevB.95.035101 for a list of all the distortion modes, except the breathing (Q_1).
[30] H. Sagayama, S. Toyoda, K. Sugimoto, Y. Maeda, S. Yamada, and T. Arima, Phys. Rev. B **90**, 241113(R) (2014).
[31] D. Okuyama, Y. Tokunaga, R. Kumai, Y. Taguchi, T. Arima, and Y. Tokura, Phys. Rev. B **80**, 064402 (2009).
[32] Y. Ito and J. Akimitsu, J. Phys. Soc. Jpn. **40**, 1333 (1976).
[33] Y. Murakami, H. Kawada, H. Kawata, M. Tanaka, T. Arima, Y. Moritomo, and Y. Tokura, Phys. Rev. Lett. **80**, 1932 (1998).
[34] M. Takata, E. Nishibori, K. Kato, M. Sakata, and Y. Moritomo, J. Phys. Soc. Jpn. **68**, 2190 (1999).
[35] H. Kuwahara, T. Okuda, Y. Tomioka, A. Asamitsu, and Y. Tokura, Phys. Rev. Lett. **82**, 4316 (1999).
[36] Y. Tokunaga, T. Lottermoser, Y. Lee, R. Kumai, M. Uchida, T. Arima, and Y. Tokura, Nat. Mater. **5**, 937 (2006).
[37] K. Momma and F. Izumi, J. Appl. Crystallogr. **44**, 1272 (2011).